IOP Publishing Journal of Physics D: Applied Physics
J. Phys. D: Appl. Phys. **40** (2007) 1447–1459 doi:10.1088/0022-3727/40/5/021

Thermal and fluid processes of a thin melt zone during femtosecond laser ablation of glass: the formation of rims by single laser pulses

Adela Ben-Yakar[1], Anthony Harkin[2], Jacqueline Ashmore[3], Robert L Byer[4] and Howard A Stone[3]

[1] Mechanical Engineering Department, The University of Texas at Austin, Austin, TX 78712, USA
[2] School of Mathematical Sciences, Rochester Institute of Technology, Rochester, NY 14623, USA
[3] Division of Engineering and Applied Sciences, Harvard University, Cambridge, MA 02138, USA
[4] Applied Physics Department, Ginzton Lab, Stanford University, CA 94305, USA

E-mail: ben-yakar@mail.utexas.edu

Received 11 December 2006, in final form 15 January 2007
Published 16 February 2007
Online at stacks.iop.org/JPhysD/40/1447

Abstract
We study the formation mechanism of rims created around femtosecond laser ablated craters on glass. Experimental studies of the surface morphology reveal that a thin rim is formed around the smooth craters and is raised above the undamaged surface by about 50–100 nm. To investigate the mechanism of rim formation following a single ultrafast laser pulse, we perform a one-dimensional theoretical analysis of the thermal and fluid processes involved in the ablation process. The results indicate the existence of a very thin melted zone below the surface and suggest that the rim is formed by the high pressure plasma producing a pressure-driven fluid motion of the molten material outwards from the centre of the crater. The numerical solutions of pressure-driven fluid motion of the thin melt demonstrate that the melt can flow to the crater edge and form a rim within the first nanoseconds of the ablation process. The possibility that a tall rim can be formed during the initial stages of the plasma is suggestive that the rim may tilt outwards towards the low pressure region creating a resolidified melt splash as observed in the experiments. The possibility of controlling or suppressing the rim formation is discussed also.

1. Introduction

Laser micromachining has been widely studied for many materials and has been extended to ultrashort laser pulses that can machine any material to very high precision at the micron scale [16]. The major benefits of an ultrashort pulse include its ability to produce a very high peak intensity ($> 10^{16}$ W cm^{-2}) and rapid deposition of energy into the material. High peak intensities allow energy delivery even into transparent high band-gap materials such as glass through nonlinear processes (multiphoton absorption, avalanche ionization etc) [15,19,20]. On the other hand, the rapid absorption of energy leads to efficient material removal before significant heat diffusion to the substrate occurs.

While the nonlinear effects and short time scales associated with ultrashort laser ablation are believed to provide a nonthermal material removal, complicated morphologies observed on micromachined glass surfaces indicate the opposite [1, 3]. Recent experiments have provided evidence for the existence of a molten region below the ablated

area, even in the femtosecond operating regime [3]. The hypothesis is that part of the absorbed laser energy remains in the bulk of the material and melts a thin layer below the ablated volume. If the lifetime of this molten layer is long enough and/or the forces acting on the liquid are large enough, the molten material will be driven from the centre to the edges of the crater, which creates an elevated rim around the ablated crater. Multiple laser pulses show that this rim formation causes a surface roughness and therefore reduces the precision of an ultrafast laser micromachining process [3].

In order to improve the quality and precision of ultrafast laser micromachining, it is important to understand, model and quantify the thermal nature of the process and any molten material rearrangement that occurs. In this paper we provide scaling arguments and an estimate for the depth of the melted layer and model its motion during the lifetime of the melt.

We first present typical experimental results of the surface morphology of craters ablated using single and multiple femtosecond laser pulses with an emphasis on the rim formation around the craters (section 2). Before presenting the modelling efforts, we discuss the ablation process and forces that might effect the rim formation (section 3). We then discuss the level of the material heating and model the variation of melt depth with time for a single laser pulse (section 4.1). Finally, we present a thin-film model to estimate the characteristic time scales of various mechanisms causing the melt to flow outwards to create the rim and show representative numerical simulations of fluid flow in a thin molten layer (section 4.2 and 4.3). We conclude with some ideas for suppressing formation of the rim (section 4.4).

2. Experimental results

Our experimental studies focus on the surface morphology of borosilicate glass (Borofloat^{TM}) ablated using single near infrared (NIR) femtosecond laser pulses. We irradiated the glass samples with 780 nm 100–200 fs pulses from a regeneratively amplified Ti : sapphire laser. The surface of the sample was positioned normal to the direction of the incident beam. We performed these experiments in air at atmospheric pressure. Following irradiation, the samples were analysed with a scanning electron microscope (SEM). The basic results were reported recently [3] and we summarize them here with some additional features as they form the basis for the theoretical and modelling considerations given in section 4.

Figure 1 presents three SEM images of crater rims produced by an average laser fluence of $F_0^{av} = 34\,J\,cm^{-2}$ (where $F_0^{av} = E_{pulse}/\pi w_0^2$, pulse energy per unit area). The laser is focused with a 250 mm focal-length lens to a spot size of about 30 μm. The first image (figure 1(*a*)) shows a thin circular rim around a nearly smooth crater following a single pulse of the laser on a flat glass substrate. It is the resemblance of this rim to a 'resolidified splash' of a molten layer that originally motivated our investigation of the dynamical processes that result in the formation of the rim.

The second image (figure 1(*b*)) shows that when a second pulse irradiates a previously formed rim a new rim is formed inside the original one. The distance between the two rims is approximately equal to the wavelength λ of the light, which suggests that diffraction of light plays an important

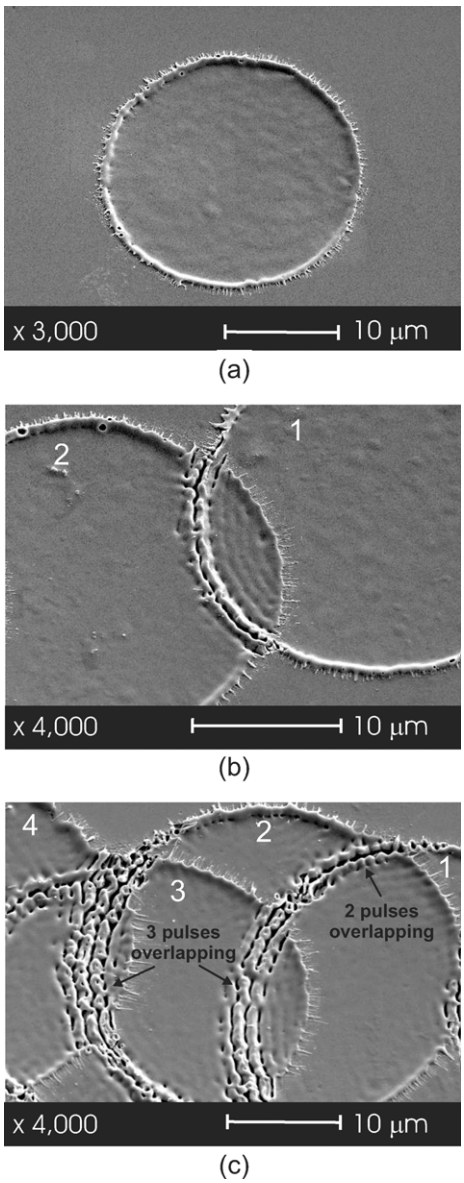

Figure 1. SEM images of crater rims generated by (*a*) one laser pulse (*b*) two overlapping laser pulses and (*c*) three overlapping laser pulses of 780 nm and 100 fs. The laser fluence was $F_0^{av} = 34\,J\,cm^{-2}$. The numbers correspond to the order of the incident laser pulses.

role [3, 4, 27]. Upon close inspection of the area between the pulses, there is a wave pattern apparently due to Fresnel diffraction-induced modulation of the second laser pulse.

When a third pulse irradiates two previously overlapping craters (figure 1(*c*)), micrometer-scale organized features appear along the rim. The smaller scale ripple-like features that are evident circumferentially along the rim, which is basically semicircular in cross-section, are presumably a manifestation of a Rayleigh capillary instability familiar from the disintegration of fluid filaments. This aspect of the surface evolution has not been studied.

In an attempt to fabricate a micro-fluidic device, we micromachined channels in a glass surface by scanning the laser beam across the surface and letting multiple laser pulses overlap. In these experiments, the laser is focused with an objective lens (Mitutoya, 5×, numerical aperture = 0.14) to a

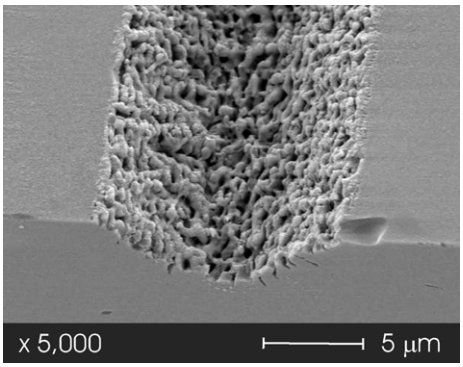

Figure 2. An SEM image of a microchannel created using 200 fs and 780 nm laser pulses of $F_0^{av} = 23\,\mathrm{J\,cm^{-2}}$ focused to a spot size of about 12 μm. The image shows the microscale surface roughness created by the rims of overlapping laser pulses when scanning the laser across the surface.

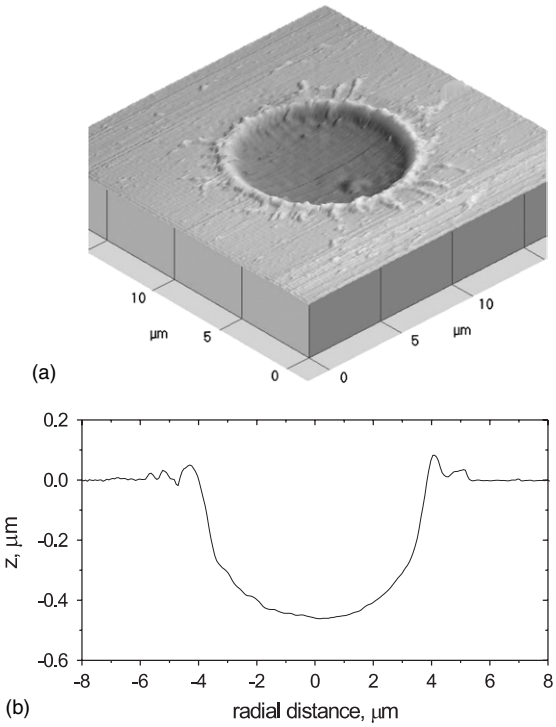

Figure 3. An AFM study of a single crater ablated with a 200 fs and 780 nm laser pulse of $F_0^{av} = 12.6\,\mathrm{J\,cm^{-2}}$. (*a*) The AFM image. (*b*) The ablation profile at the centre-line of the crater. The radius of the beam spot size is $w_0 = 5.9\,\mu$m.

spot size of about 12 μm. As shown in figure 2, the interplay between rim formation and diffraction results in a perceptible surface roughness inside the channels.

Figure 3 shows a detailed AFM study of a single crater. The rim is raised by about 50–100 nm above the surface and the maximum depth of the ablated crater, h_a, is about 450 nm. The ablation depth, h_a, depends linearly on the logarithm of the average laser fluence, F_0^{av}, according to [2]

$$h_a = \alpha_{eff}^{-1} \ln\left(\frac{F_0^{av}}{F_{th}}\right), \qquad (1)$$

where $F_{th} = 1.7\,\mathrm{J\,cm^{-2}}$ is the minimum fluence to initiate ablation (threshold fluence) in borosilicate glass. The slope

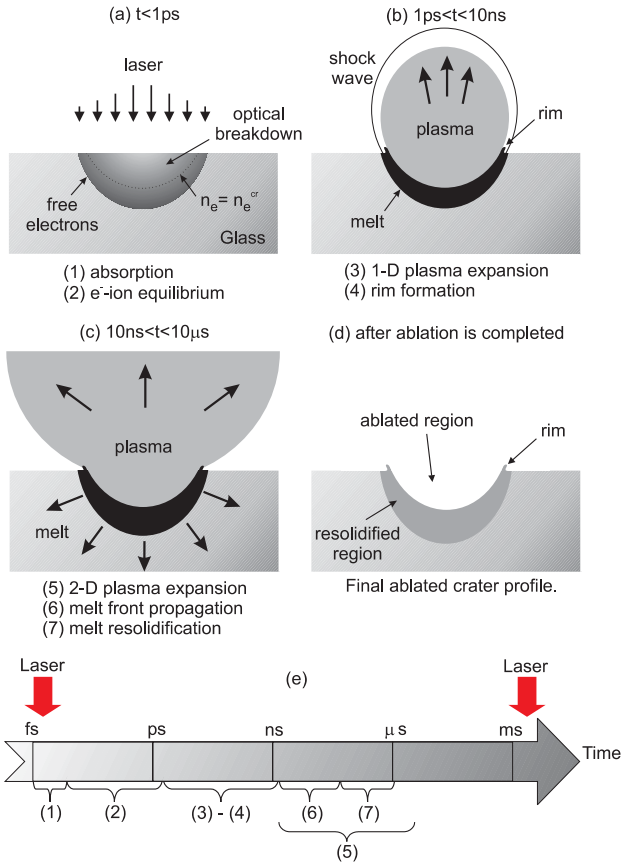

Figure 4. A schematic description of ablation process of glass with a femtosecond laser pulse (*a*)–(*d*) and time scales associated with various processes (*e*).

(This figure is in colour only in the electronic version)

of this linear relationship yields $\alpha_{eff}^{-1} = 238$ nm. This parameter represents the distance where the laser fluence decreases to $1/e$ of its value and thus can be interpreted as the 'effective optical penetration depth' in accordance with the Beer–Lambert absorption law. We use these measured data in our heat transfer calculations in section 4.1.

In order to understand and control the micromachining process using ultrafast lasers, it is necessary to investigate the formation mechanism of the surface microfeatures. To address these issues, we examine the rim formation of a single laser pulse as the main focus of this paper.

3. Physical processes

Ultrafast laser ablation of dielectric materials such as glass involves a number of processes, including nonlinear absorption, plasmas, shock propagation, melt propagation and resolidification. Each of these processes has a different time scale and can roughly be grouped into three different time domains as illustrated in figure 4.

In the first picosecond (figure 4(*a*)), part of the incident laser energy is absorbed by electrons through multiphoton and avalanche ionization [19, 20] and then transferred to the lattice on the time scale of few picoseconds. As the electrons and ions thermally equilibrate, a high-pressure and high-temperature plasma is formed above the surface. At early times

(less than 10 ns, figure 4(*b*)), the plasma expands primarily in the direction perpendicular to the target surface [31]. In the later stages (figure 4(*c*)), the plasma expands in both the lateral and perpendicular directions and removes the ablated material from the surface.

A large portion of the absorbed energy is used by the expanding plasma to move into the ambient gas [29]. A small portion of it remains in the target as thermal energy. The thermal energy deposited in the bulk of the glass forms a transient shallow molten zone below the expanding plasma [3]. Ladieu *et al* [13], for example, measured that about 8% of the incoming energy was thermalized and transmitted to the undamaged part of a quartz material when irradiated with a 100 fs laser pulse. During plasma expansion, the front of the molten material propagates into the bulk as a result of the heat diffusion. When the temperature of the melt decreases below the melting temperature the melt resolidifies. The forces acting on the molten material drive the liquid from the centre to the edges of the crater during the melt lifetime and create an elevated rim around the ablated crater as the melt resolidifies.

Two main forces might affect the flow of a molten layer below the expanding plasma: (1) thermocapillary forces (Marangoni flow) and (2) forces exerted by the pressure of the plasma above the surface. Thermocapillary flow is induced by the temperature gradient on the surface which is expected to follow the Gaussian beam intensity profile of the laser. In studies of laser texturing of silicon surfaces in the absence of ablation, the rim formation was attributed to the thermocapillary flow in thin films created by nanosecond laser pulse heating [21,30]. The temperature gradient on the surface creates surface tension gradients that drives material from the hot centre to the cold periphery. This response is expected in most materials where the surface tension, γ, decreases as the fluid gets hotter ($\mathrm{d}\gamma/\mathrm{d}T < 0$). However, in the case of glass $\mathrm{d}\gamma/\mathrm{d}T$ is positive [12]. Consequently, such a thermocapillary flow in laser irradiated glass surfaces would actually drive fluid from the cold periphery to the hot centre of the melt in contrast to what was observed in our experiments. In addition, the effect of thermocapillary flow in glass is expected to be negligible because of its high viscosity, which leads to a flow time scale much longer than the typical melt time scale, as detailed further below.

On the other hand, a hydrodynamic force due to the pressure gradients exerted by the plasma onto the molten material might play an important role in the rim formation. A gradient of ablation pressure on the molten surface can induce a lateral melt flow to the periphery [26]. The pressure gradients are particularly large at the plasma/air interface which should be close to the edges of the molten layer. Because of these large pressure gradients, we expect a melt flow to the periphery and rise of a thin rim at the edges of the melted surface much like a splash of a liquid. In this paper, we provide a two-dimensional model of the pressure-driven flow processes and give the time evolution for the profile of the melt surface.

4. Theoretical modelling and discussion

Simulation of all the physical process involved in femtosecond laser ablation of glass requires a rather complicated and time consuming numerical solution. In this paper, we propose simple analytical and numerical models that can qualitatively address the thermal and flow processes associated with the first laser pulse. The goal is to identify the physical processes involved in the formation of rim around the laser ablated crater and suggest ways to eliminate it.

The rim formation is associated with the fluid dynamics of the molten layer and the properties of the forces exerted by the plasma that controls its dynamics. We first estimate the properties of the molten layer (its thickness and its variation in time) through heat transfer calculations (section 4.1). A thin-film model of the molten surface layer is then introduced to explore the temporal evolution of the melt surface (section 4.2).

4.1. Heat transfer calculations

In this section, our goal is to estimate the initial thickness of the molten layer and to predict the variation of this thickness with time. These properties are directly related to the amount of the absorbed energy that remains in the bulk of the material as heat, namely, to the thermalized energy. Let us first estimate the amount of the energy that is absorbed by the material.

4.1.1. Absorptivity (A). The incident laser energy delivered to the sample is either reflected, transmitted or absorbed. Absorptivity, A, refers to the fraction of the incoming energy that is absorbed by the material. The absorptivity of a dielectric material depends on the intensity of the laser irradiation and varies with time during the duration of the laser pulse. When glass is exposed to high intensity ultrashort pulses, its reflectivity increases with time as the plasma density increases [19]. Once the critical surface plasma density is formed, any further incident laser energy is reflected back from the surface due to an induced skin effect. Perry *et al* [19] showed that when the incident laser fluence is much larger than the threshold ($F_0^{\mathrm{av}} > 10$–$20F_{\mathrm{th}}$ where $F_{\mathrm{th}} \approx 2\,\mathrm{J\,cm^{-2}}$ for fused silica), a plasma with a critical density can be achieved early in the pulse and a large portion of the energy is reflected. At a laser fluence of $20\,\mathrm{J\,cm^{-2}}$, they estimated the reflectance to be about 60% (for $\lambda = 1064$ nm and $\tau_{\mathrm{p}} = 350$ fs). The other 40% of the incident energy is either absorbed or transmitted.

In a recent study, Chowdhury *et al* [7] measured both the reflectivity and transmissivity of a single 90 fs, 800 nm pulse in fused silica. As predicted by theory, they found that the transmissivity drops and the reflectivity rises as the incident intensity is increased. On the other hand, the absorptivity increases sharply near the threshold fluences and remains constant (about $A = 0.35 \pm 0.03$) for fluences between 5 and $25\,\mathrm{J\,cm^{-2}}$. Therefore, in our calculations we assume that the absorptivity is between $A = 0.3 - 0.4$.

4.1.2. Thermalized fluence (F_{heat}). The incident laser beam is absorbed initially by electrons through multiphoton and avalanche ionization. Dissipation of the energy absorbed by the electrons begins only after the laser pulse is gone. The absorbed energy is transferred from the high energy electrons to the lattice through electron–phonon scattering within the region of energy deposition. This happens within the first 10–20 ps. Substantial heat diffusion begins only after few tens of nanoseconds. In the case of femtosecond laser ablation of glass, a rather complicated and time consuming numerical

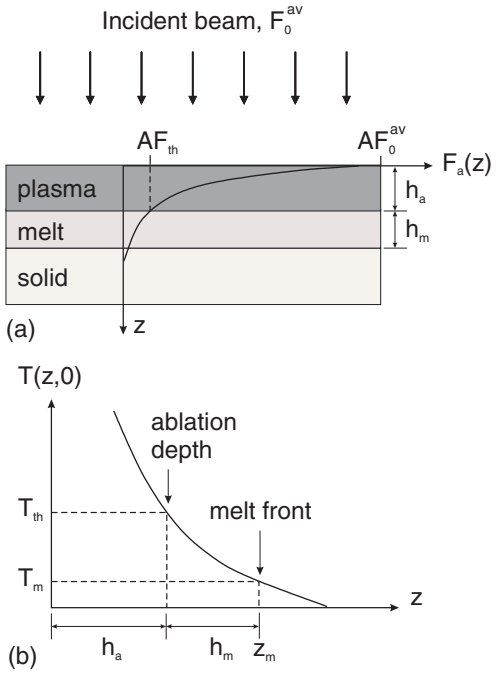

Figure 5. (*a*) Initial deposition of the absorbed laser fluence, AF_0^{av}, according to the Beer-Lambert law for a uniform laser beam distribution. (*b*) A sketch of the resulting initial temperature distribution inside the material.

solution is required to estimate the partition of the absorbed laser energy. In our calculations, we propose to use an 'effective optical light penetration depth' measured in our experiments to estimate the fraction of the incoming laser energy deposited in the glass as heat (thermal energy).

The absorbed laser energy is deposited in a layer defined by the penetration of light. A convenient means to quantify the penetration depth of light is the Beer–Lambert law, which assumes that the light intensity is attenuated exponentially with depth z. Then, the attenuation of the absorbed laser fluence as a function of depth is given by

$$F_a(z) = AF_0^{av} \exp\left(-\frac{z}{\alpha_{eff}^{-1}}\right), \tag{2}$$

where the surface absorptivity is $A = 0.3$–0.4 and the effective optical penetration depth is $\alpha_{eff}^{-1} = 238$ nm, as measured in our previous experiments (see equation (1)) [2].

Figure 5 illustrates this exponential decay of the laser fluence with depth for a uniform incident laser beam. There are three distinct layers for the absorption depth. The first layer represents the ablation region. Within the ablation depth (h_a), the fluence absorbed at the surface (AF_0^{av}) drops to the ablation threshold value (AF_{th}). In this layer, a high pressure and temperature plasma is formed. The second layer represents the molten region. When the fluence drops below the ablation threshold, optical breakdown of glass cannot occur (electron number density is below the critical value) and the absorbed fluence goes into melting of the material. The third layer represents the solid region in which the heating is insufficient to melt the material.

The variation of the absorbed laser fluence with depth can be rewritten in terms of F_{th} and h_a by combining equations (1) and (2),

$$F_a(z) = AF_{th} \exp\left(\frac{h_a - z}{\alpha_{eff}^{-1}}\right), \tag{3}$$

where $z = 0$ corresponds to the location of the flat surface. At the ablation depth, $z = h_a$, the fluence drops to $F(h_a) = AF_{th}$.

Assuming that laser fluence penetrating beyond the ablation depth, $z \geqslant h_a$, goes into heating of the bulk, the amount of thermalized fluence is about $F_{heat} = AF_{th} = 0.5\,\mathrm{J\,cm^{-2}}$ for $A = 0.3$ (about 1.5 % of the incident laser energy). Thus, we find that a fixed amount of laser fluence heats the material below the ablation crater independent of the incident laser fluence. This means that below the ablation crater, a melt layer of a constant thickness is formed even if the laser beam profile has a Gaussian distribution.

4.1.3. Initial melt thickness ($h_{m,0}$). After the laser energy is absorbed by the electrons within the pulse duration of about 100 fs, electrons transfer their energy to ions within several picoseconds. Since the glass materials do not have a latent heat of melting, all of the thermalized energy goes to increase in lattice temperature; $\Delta T \propto F_a/(\rho C_p \alpha_{eff}^{-1})$. Thus, the fluence deposition described by equation (3) produces an initial temperature distribution in the glass, $T_0(z)$, with an exponential profile

$$T_0(z) - T_\infty = \frac{AF_{th}}{\rho C_p \alpha_{eff}^{-1}} \exp\left(\frac{h_a - z}{\alpha_{eff}^{-1}}\right), \tag{4}$$

where T_∞ is the ambient temperature, ρ is the density of the substrate and C_p is the heat capacity. Melting of borosilicate glass occurs when the local temperature exceeds the temperature, $T_m \approx 1500$ K [9]. The value T_m is the working point temperature of glass, defined as the temperature at which the glass can readily be formed, which corresponds to a viscosity of approximately 10^3 Pa s. We can therefore calculate the initial melt thickness, $h_{m,0} = z_{m,0} - h_a$, from $h_{m,0} = \alpha_{eff}^{-1} \ln(AF_{th}/(T_m - T_\infty)\rho C_p \alpha_{eff}^{-1})$ where $C_p = 1250\,\mathrm{J\,kg^{-1}\,K^{-1}}$ (see the thermophysical properties of glass in table 1); we have chosen to evaluate all physical parameters at the mean temperature of 900 K. This calculation yields an initial molten layer thickness of $h_{m,0} \approx 440$ nm for $A = 0.3$ and $h_{m,0} \approx 505$ nm for $A = 0.4$.

4.1.4. Variation of melt thickness with time ($h_m(t)$). Following the cessation of ultrafast energy input, the melting process continues as the heat flows out of the region where the initial energy is deposited. Diffusion of the thermal energy determines the movement of the melting front and therefore the variation of the melt thickness.

We can easily calculate the heat flow out of the region where the initial energy is deposited by solving a one-dimensional (1D) heat conduction equation with an initial temperature profile described by equation (4). The cooling at the top of the melt zone is assumed to be negligible because of the presence of the high temperature plasma. During the expansion, the plasma cools in tens of microseconds from some very high initial temperature to the ambient temperature. Hence, all of the heat loss is assumed to take place through the

Table 1. Thermophysical properties of borosilicate glass (Borofloat™). The chemical composition includes 81% SiO_2, 13%B_2O_3, 2%Al_2O_3 and 4%Na_2O.

Property	Symbol	Units	Values
Density [9]	ρ	kg m^{-3}	2.23×10^3
Melting temperature [9][a]	T_m	K	1500
Viscosity [9]	μ	Pa s	$\approx 10^3$ (at 1500 K) $\approx 10^2$ (at 2000 K) $1 - 10$ (> 2500 K)
Surface tension [5]	γ	N m^{-1}	0.28 (at 300 K)
Temperature coefficient of surface tension [12]	γ_T	N m^{-1} K^{-1}	3.4×10^{-5}
Thermal conductivity [5][b]	k	W m^{-1} K^{-1}	1.25 (at 300 K) 1.6 (at 600 K) 4.5 (at 900 K) 42.0 (at 1500 K)
Specific heat [8][b]	C_p	J kg^{-1} K^{-1}	746 (at 300 K) 1000 (at 600 K) 1250 (at 900 K) 1320 (at 1500 K)
Thermal diffusivity[b]	D	m^2 s^{-1}	0.75×10^{-6} (300 K) 0.72×10^{-6} (600 K) 1.60×10^{-6} (900 K) 14.3×10^{-6} (1500 K)

[a] T_m is the working point temperature of glass, defined as the temperature at which the glass can readily be formed and has a viscosity of approximately 10^3 Pa s.
[b] In the heat conduction calculations, we used data at an average temperature of 900 K, which is an average between $T_\infty = 300$ K and $T_m = 1500$ K.

solid, as the rearrangement of the molten layer takes place on shorter time scales.

The one-dimensional heat conduction model can then be described by

$$\frac{\partial T}{\partial t} = \frac{\partial}{\partial z}\left(D\frac{\partial T}{\partial z}\right), \qquad z > h_a, \tag{5}$$

$$\frac{\partial T}{\partial z} = 0 \qquad \text{at } z = h_a, \tag{6}$$

$$T = T_\infty \qquad \text{as } z \to \infty, \tag{7}$$

$$T(z,0) = T_\infty + T_{th} e^{-(z-h_a)/\alpha_{eff}^{-1}} \qquad \text{at } t = 0, \tag{8}$$

where $T_{th} = AF_{th}/\rho C_p \alpha_{eff}^{-1}$. As a first approximation, we assume that the heat capacity, C_p, the thermal conductivity, k, the density, ρ, and therefore the thermal diffusivity, $D = k/\rho C_p$, are constants at an average temperature of 900 K.

To find an analytical solution for this heat conduction problem, nondimensionalize variables as

$$\bar{T} = \frac{T - T_\infty}{T_{th}}, \qquad \bar{z} = \frac{z - h_a}{\alpha_{eff}^{-1}},$$
$$\bar{t} = \frac{D}{(\alpha_{eff}^{-1})^2} t. \tag{9}$$

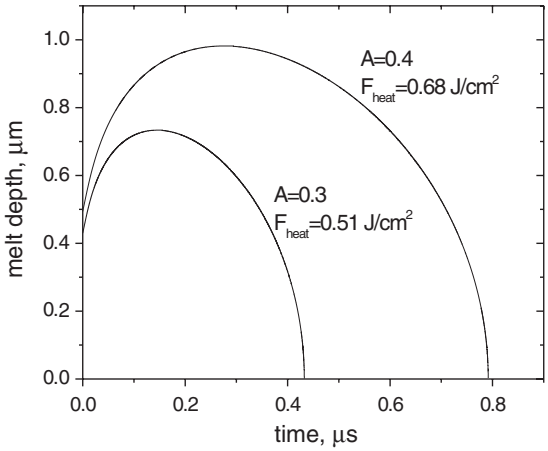

Figure 6. Time variation of melt depth, $h_m(t)$, at the centre-line of the crater for two different absorptivities, $A = 0.3$ and 0.4, and for their corresponding thermalized fluences of $F_{heat} = 0.51$ and 0.68 J cm^{-2}. The calculations are performed assuming constant thermophysical properties at an average temperature of 900 K.

The nondimensional problem statement is then

$$\frac{\partial \bar{T}}{\partial \bar{t}} = \frac{\partial^2 \bar{T}}{\partial \bar{z}^2}, \qquad \bar{z} > 0, \tag{10}$$

$$\frac{\partial \bar{T}}{\partial \bar{z}} = 0 \qquad \text{at } \bar{z} = 0, \tag{11}$$

$$\bar{T} = 0 \qquad \text{as } \bar{z} \to \infty, \tag{12}$$

$$\bar{T}(\bar{z},0) = f(\bar{z}) = e^{-\bar{z}}, \tag{13}$$

which has the solution

$$\bar{T}(\bar{z},\bar{t}) = \frac{1}{\sqrt{4\pi\bar{t}}}\int_0^\infty f(\zeta)\left[e^{-(\bar{z}+\zeta)^2/4\bar{t}} + e^{-(\bar{z}-\zeta)^2/4\bar{t}}\right]d\zeta. \tag{14}$$

When $f(\zeta) = e^{-\zeta}$, this can be expressed in terms of the complementary error function, erfc(s), as

$$\bar{T}(\bar{z},\bar{t}) = \frac{e^{\bar{t}}}{2}\left[e^{\bar{z}}\text{erfc}\left(\frac{\bar{z}+2\bar{t}}{\sqrt{4\bar{t}}}\right) + e^{-\bar{z}}\text{erfc}\left(\frac{-\bar{z}+2\bar{t}}{\sqrt{4\bar{t}}}\right)\right]. \tag{15}$$

We can now calculate the temperature distribution in the material below the plasma using the analytical solution given in equation (15). The melt depth, $h_m = z_m - h_a$, as a function of time is obtained by solving $T(z_m, t) = T_m$. A plot of melt depth versus time is shown in figure 6 for two different aborptivities, $A = 0.3$ and 0.4. The numerical results show that the melt front propagates into the material for about 100–200 ns as the heat diffuses out of the initial melt depth and then solidification (retraction of the melt front) begins. These calculations provide us estimates for the order of magnitude of two important characteristic scales of the melt zone:

- The average melt depth, $\langle h_m \rangle$, varies between 0.6 and 0.8 μm.
- The average melt lifetime, $\langle t_m \rangle$, varies between 0.4 and 0.8 μs.

These estimates obtained using the 1D heat conduction model represent a good approximation for studying the melt variation at the centre-line of the ablation crater. We have also calculated

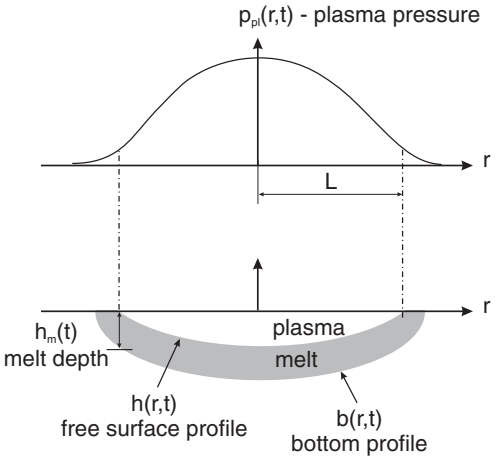

Figure 7. Description of parameters used in the thin film model to calculate the evolution of the free surface of the melt.

the variation of melt depth using a more comprehensive 2D heat conduction model, which resulted in similar results to the 1D problem from the order of magnitude of the average melt thickness and its lifetime. As we will discuss in the next section, the numerical simulation of thin melt flow indicates that the rim formation is most probably formed over a nanosecond time scale. During this time the melt thickness does not vary significantly and can be assumed to be constant with a value of its initial thickness. Therefore, we present here only the 1D heat conduction calculations, which are sufficient for providing an estimate for the variation of the melt properties for the purpose of this study.

4.2. Fluid dynamics calculations

4.2.1. Thin-film model. In this section, we examine the hydrodynamic conditions under which a crater partially filled with molten glass can form rims reaching the heights measured in experiments. For this purpose, we develop a two-dimensional (2D) model of the fluid motion, in the circular geometry representative of the experiments, as illustrated in figure 7. It is natural to work with cylindrical coordinates. The free surface of the molten glass is described by $h(r, t)$ and the boundary between the liquid and the solid substrate, namely the bottom profile of the molten glass, is given by the profile $b(r, t)$.

The shape of the thin liquid film evolves owing to variations in the surface tension $\gamma(r, t)$ along the free surface and because of the very high pressure $p_{\mathrm{pl}}(r, t)$ of the plasma above the free surface. Because the melted region has a typical height much less than the typical width of the laser ablated craters, the lubrication approximation (see appendix A) can be used to obtain an evolution equation for the time-dependent profile of the free surface $h(r, t)$:

$$\frac{\partial(h-b)}{\partial t} + \frac{1}{r}\frac{\partial}{\partial r} r \Bigg[\underbrace{\frac{(h-b)^2}{2\mu}\frac{\partial \gamma}{\partial r}}_{\text{Marangoni}} - \underbrace{\frac{(h-b)^3}{3\mu}\frac{\partial p_{\mathrm{pl}}}{\partial r}}_{\text{Pressure}} + \underbrace{\frac{(h-b)^3}{3\mu}\frac{\partial}{\partial r}\left(\frac{\gamma}{r}\frac{\partial}{\partial r}\left(r\frac{\partial h}{\partial r}\right)\right)}_{\text{Curvature}} \Bigg] = 0, \tag{16}$$

where μ is the liquid viscosity and the different flux contributions have been labelled. The first term in brackets accounts for motion caused by the surface tension gradients due to the uneven heating of the surface (thermocapillary or Marangoni-driven flow). The second term accounts for the motion due to the pressure gradients exerted by the plasma onto the molten material, and the third term in (16) represents surface tension effects, which enter as the product of surface tension and surface curvature (the latter has been linearized).

4.2.2. Comparison of flow times scales. When a surface temperature distribution, $T_{\mathrm{s}}(r)$, is imposed, then the surface tension varies according to

$$\frac{\mathrm{d}\gamma}{\mathrm{d}r} = \frac{\mathrm{d}\gamma}{\mathrm{d}T_{\mathrm{s}}}\frac{\mathrm{d}T_{\mathrm{s}}}{\mathrm{d}r}. \tag{17}$$

We assume $\gamma_T = \mathrm{d}\gamma/\mathrm{d}T_{\mathrm{s}}$ is constant and neglect the effect of temperature variations on the viscosity. Using equation (16) we can estimate characteristic time scales associated with the Marangoni flow (τ_{M}), and the pressure-driven flow (τ_{p}),

$$\text{Marangoni flow}: \qquad \tau_{\mathrm{M}} \approx \frac{\mu L^2}{\gamma_T T_{\mathrm{m}} \langle h_{\mathrm{m}} \rangle}, \tag{18}$$

$$\text{Pressure-driven flow}: \qquad \tau_{\mathrm{p}} \approx \frac{\mu L^2}{\langle p_{\mathrm{pl}} \rangle \langle h_{\mathrm{m}} \rangle^2}, \tag{19}$$

where $\langle h_{\mathrm{m}} \rangle$ is an average melt depth, L is a typical radial dimension and $\langle p_{\mathrm{pl}} \rangle$ is an average plasma pressure. The thermophysical properties of borosilicate glass are summarized in table 1. For an average melt depth of $\langle h_{\mathrm{m}} \rangle \approx 1\,\mu$m, as estimated in the heat transfer calculation in section 4.1, a typical crater radius of $L = 10\,\mu$m, (comparable with the radius of the Gaussian laser pulse) and an average plasma pressure of $\langle p_{\mathrm{pl}} \rangle \approx 1000$ atm (the typical plasma pressure drops from millions of atmospheres to about 100 atm during the first 10 ns of its expansion [19]), we obtain

$$\frac{\tau_{\mathrm{M}}}{\tau_{\mathrm{p}}} = O\left(\frac{\langle p_{\mathrm{pl}} \rangle \langle h_{\mathrm{m}} \rangle}{\gamma_T T_{\mathrm{m}}}\right) \approx 10^3. \tag{20}$$

Hence the characteristic time scale for Marangoni flow is about three orders of magnitude longer than that of pressure-driven flow, and $\tau_{\mathrm{p}} \ll \tau_{\mathrm{M}}$ even if the peak pressure is lowered more than a factor of ten. It is clear from this estimate that the large plasma pressure above the free surface acts to move the fluid much more quickly than do the surface tension gradients.

This mechanism for rim formation contrasts with that in laser texturing of silicon surfaces in the absence of ablation, which is attributed to the Marangoni flow in thin films created by nanosecond laser pulse heating [21]. The idea that thermocapillary effects do not contribute to the observed formation of a rim at the edge of the melt zone in our experiments is supported by the observation that the surface tension coefficient of borosilicate glass is positive [12] in contrast to the usual negative values of the most pure liquids. Therefore, as discussed earlier, thermocapillary (Marangoni) flow in laser irradiated glass surfaces would be expected to drive fluid from the cold periphery to the hot centre of the melt, which is not what is observed in the experiments shown in figure 1.

4.2.3. Verification of assumptions. There are three assumptions needed to justify the use of equation (16): (i) the film must be thin, i.e. $\langle h_m\rangle/L \ll 1$. (ii) The Reynolds number $\mathcal{R}_e$ for the film flow (see appendix A) must be small, $\mathcal{R}_e = \rho\langle h_m\rangle^3\langle p_{pl}\rangle/(\mu^2 L) \ll 1$. (iii) The flow must be quasi-steady which requires the time for 'viscous diffusion' across the thin layer, $\rho\langle h_m\rangle^2/\mu$, to be small compared with the time scale for film evolution.

We now verify these three assumptions used to obtain equation (16). First, since $\langle h_m\rangle \approx 1\,\mu$m and $L \approx 10\mu$m, then $\langle h_m\rangle/L \ll 1$ and the 'thinness' approximation is reasonably well satisfied. In fact, errors in using equation (16) are $O\left((\langle h_m\rangle/L)^2\right)$, which further justifies the use of the lubrication approximation for this thin-film flow. Second, we require that the effective Reynolds number, $\mathcal{R}_e$, for the film flow must be small. Using typical parameter values and viscosity $\mu = 10$ Pa s at $T = 2500$ K, we obtain

$$\mathcal{R}_e = O\left(\frac{\rho\langle h_m\rangle^3\langle p_{pl}\rangle}{\mu^2 L}\right) \approx 10^{-4}. \tag{21}$$

Note that even if the pressure gradient that drives the flow was increased three orders of magnitude, the low-Reynolds-number assumption, equation (21), is still satisfied. Finally, the third assumption requires that the viscous effects must act quickly to establish the velocity profile across the thin region. This time is $O(\rho\langle h_m\rangle^2/\mu) \approx 10^{-10}$ s, which is much faster than the time scale, τ_p, of fluid motion. Hence, the three principal assumptions in the fluid dynamics calculation are verified.

4.3. Numerical results and discussion for pressure-driven flow

To perform numerical simulations of the evolution of the molten glass we first nondimensionalize the time, length, height and plasma pressure by characteristic values

$$S = t/\tau_p, \qquad R = r/L, \qquad H = h/\langle h_m\rangle,$$
$$B = b/\langle h_m\rangle, \qquad P_{pl} = p_{pl}/\langle p_{pl}\rangle. \tag{22}$$

Since the key estimate of the previous section, equation (20), indicates plasma pressure gradients primarily drive the fluid flow we can neglect the Marangoni term from equation (16), and arrive at the following nondimensional evolution equation for the free surface height, $H(R, S)$,

$$\frac{\partial(H-B)}{\partial S} - \frac{1}{R}\frac{\partial}{\partial R}R\left[\frac{(H-B)^3}{3}\frac{\mathrm{d}P_{pl}}{\mathrm{d}R} + \frac{(H-B)^3}{3}\frac{\partial}{\partial R} \times\left(\frac{\Lambda}{R}\frac{\partial}{\partial R}\left(R\frac{\partial H}{\partial R}\right)\right)\right] = 0. \tag{23}$$

The nondimensional parameter Λ is given by

$$\Lambda = \frac{\gamma\langle h_m\rangle}{\langle p_{pl}\rangle L^2} \approx 10^{-5}. \tag{24}$$

Even though Λ is small, we will keep the curvature term in the numerical simulations.

To solve the time evolution of the free surface using equation (23), we need to provide the initial state of the interfaces $H(R, 0)$ and $B(R, 0)$ and the time evolution of the plasma pressure profile $P_{pl}(R, S)$.

4.3.1. Initial profiles of the interfaces. There are three different interfaces in this problem: (a) melt–plasma interface (the free-surface, $H(R, S)$), (b) melt–solid interface (the bottom profile, $B(R, S)$) and (c) melt–air interface that becomes melt–plasma later when the plasma above the crater expands radially.

We describe the initial profiles of melt–plasma and melt–solid interfaces based on the measured profile of the ablation crater (see figure 3). Due to nonlinear absorption properties of glass exposed to femtosecond laser pulses, the ablation profile is not linearly related to the Gaussian distribution (r^2 dependence) of the incoming laser beam. The divergence from the Gaussian profile is especially pronounced at the edges where the absorptivity varies significantly. The ablation profile depends mainly on two parameters: (a) laser fluence distribution (Gaussian) and (b) the absorption properties of glass that depends nonlinearly on the laser intensity. One can estimate how the absorptivity varies with the radial distribution of a Gaussian laser intensity or fluence. Alternatively, one can describe an 'effective laser fluence' profile assuming a constant absorptivity by matching the resultant ablation crater profile to the measured one. We choose to follow the second method in describing the initial profiles of the interfaces.

The radial fluence (energy/area) distribution of a Gaussian beam is given by

$$F(r) = F_0^{peak}\exp\left(-\frac{2r^2}{w_0^2}\right), \tag{25}$$

where $F_0^{peak} = 2E_{pulse}/\pi w_0^2 = 2F_0^{av}$. The radial distribution of ablation depth can then be described using equation (1)

$$h_a(r) = \alpha_{eff}^{-1}\ln\left(\frac{F(r)}{2F_{th}}\right). \tag{26}$$

Figure 8 compares the ablation depth contour for a Gaussian beam profile as calculated using equation (26) with the measured data presented in figure 3. While the centre of the crater follows the Gaussian laser beam distribution, the crater edges do not. We have found that an effective fluence profile in the form of

$$F_{eff}(r) = F_0^{peak}\exp\left\{-2\left[\left(\frac{r}{w_0}\right)^2 + \left(\frac{r}{0.7w_0}\right)^8\right]\right\} \tag{27}$$

fits best to the measured crater profile and is used to describe the initial profile for the free surface of the melt in the numerical simulations. By combining equations (26) and (27), the *initial free surface profile* can be presented in the following non dimensional form:

$$H(R, 0) = \frac{\alpha_{eff}^{-1}}{\langle h_m\rangle}\left\{\ln\left(\frac{F_0^{av}}{F_{th}}\right) - 2\left[R^2 + \left(\frac{R}{0.7}\right)^8\right]\right\}. \tag{28}$$

The melt–solid interface (the bottom profile, $B(R)$) can then be described easily assuming a constant thickness of molten layer underneath the ablation crater profile. In the discussion of energy deposition, we assumed that the incident laser beam and the resulting initial temperature distribution inside the glass material attenuate exponentially with depth. Accordingly we found that the threshold fluence for melting is about $F_{heat} = AF_{th}$ that results in a constant melt thickness below the expanding plasma. Thus, as a first approximation

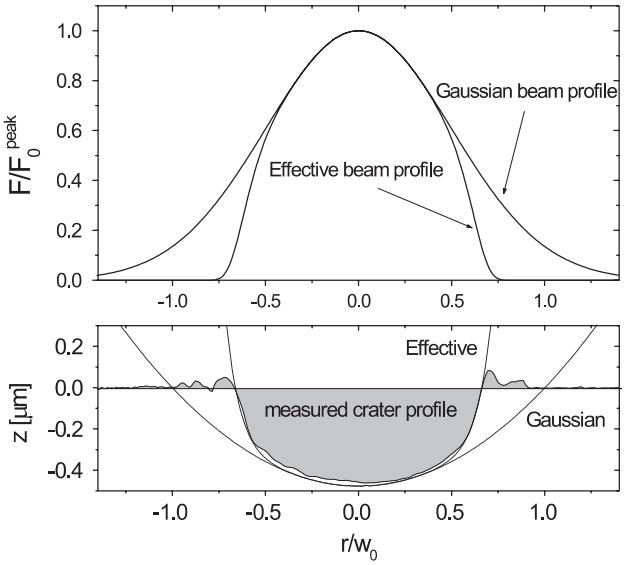

Figure 8. Plots of laser ablation depths, h_a, calculated for (*a*) a Gaussian beam profile and (*b*) an effective laser beam profile (equation 28). The estimated ablation crater profiles are compared with the measured ablation depth given in figure 2. The ablation crater profile as obtained by the effective laser fluence fits best to the measured crater profile and is used as the initial profile for the free surface of the melt in the numerical simulations.

the initial thickness of the molten glass can be assumed constant below the ablation crater and is equal to $h_{m,0} = \alpha_{eff}^{-1} \ln(T_{th}/(T_m - T_0))$ where $T_{th} = AF_{th}/\rho C_p \alpha_{eff}^{-1}$. The *initial bottom profile* can thus be presented as

$$B(R,0) = H(R,0) - \frac{h_{m,0}}{\langle h_m \rangle}. \tag{29}$$

In our calculations we use $h_{m,0} = 462\,\text{nm}$ for an average absorptivity $A = 0.35$. We will next show that the rim is most probably formed in a nanosecond time scale during which the melt thickness does not vary significantly and can be assumed to be constant with a value of its initial thickness. Thus, we assume that the bottom profile is independent of time $B(R)$.

4.3.2. Plasma pressure profile. The dynamics of the plasma is very complicated and resolving the details of its temporal and spatial evolution requires extensive 3D numerical simulations. Especially during the first 100 ps, the plasma is in a highly nonequilibrium state and it should be approached with a molecular dynamics type of simulations [22, 32, 33].

In the literature, only a limited number of studies have attempted to investigate the fs-laser induced plasma dynamics [10, 14]. Among these studies, Perry *et al* [19] solved the problem using one-dimensional Euler–Lagrangian code. Their calculations provide a valuable insight for the temporal variation of plasma pressure during the first few nanoseconds. Numerical data of Perry *et al* [19] is shown in figure 9 together with some other experimental measurements of the average plasma pressure [6, 28]. We fitted the data of Perry *et al* [19] with an exponential curve, in the form of $p_{pl} = at^c$, for describing the time evolution of the maximum plasma pressure in our calculations and obtained $a = 10^{-6.57}$ and $c = 1.57$ for metric units of pressure.

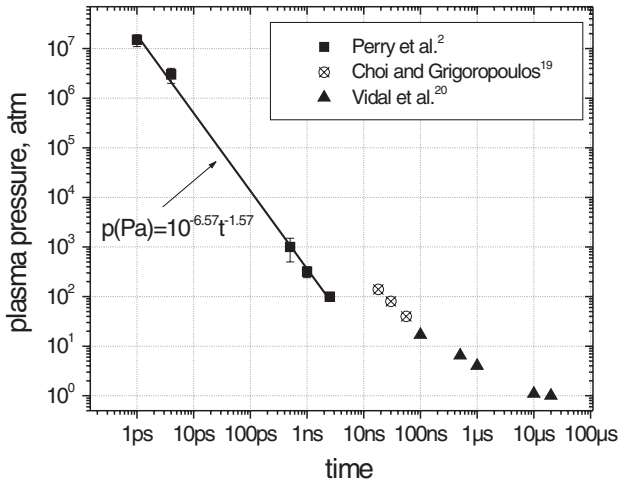

Figure 9. Plasma pressure data from the literature [19, 6, 28]. Temporal variation of the plasma pressure used in our calculations is estimated using a curve fit to Perry *et al* 's calculations [19] using SI units.

For describing the radial distribution of the plasma pressure we consider the fact that the thermalization of the absorbed laser energy takes a few picoseconds. This time is too short for significant expansion to occur. Thus, the starting point is solid density material with an initial temperature determined by the amount of absorbed energy [23]. For a constant density plasma, the pressure variation corresponds to the temperature distribution. The radial distribution of temperature, thus that of pressure, is determined by the profile of the absorbed laser fluence, namely by the profile of the effective laser fluence.

Assuming that the radial distribution of plasma pressure is in accordance with the effective laser fluence, we obtain the following nondimensional pressure distribution:

$$P_{pl}(R,S) = \frac{a\tau_p^{-c} S^{-c}}{\langle p_{pl} \rangle} \left\{ -2 \left[R^2 + \left(\frac{R}{0.7} \right)^8 \right] \right\}. \tag{30}$$

At the early times the plasma expansion is one directional, thus the plasma is confined within the ablated crater. At the later times, the plasma expansion is three dimensional and the above description of the confined plasma profile will be inadequate. The problem is obviously much more complex than how we approach it here. However, this model for the pressure distribution presents a good qualitative and quantitative description of the plasma variation for the first nanoseconds of the ablation process.

4.3.3. Evolution of the free surface: numerical results. We next numerically explore the behaviour of solutions of equation (23) with equation (30) for the time-dependent pressure distribution. The rim height is the feature of the solution in which we are most interested. More specifically, we investigate whether plasma pressure above the molten glass can apply large enough forces to form a rim around the ablation crater during the lifetime of melt and high pressure 1D plasma.

Figure 10 presents a numerical solution for pressure-driven melt flow of the free surface for glass viscosity of $\mu = 2\,\text{Pa s}$. The upper plot describes the pressure radial distribution according to equation (30) and the bottom plot shows the evolution of the free surface after $t = 1\,\text{ns}$.

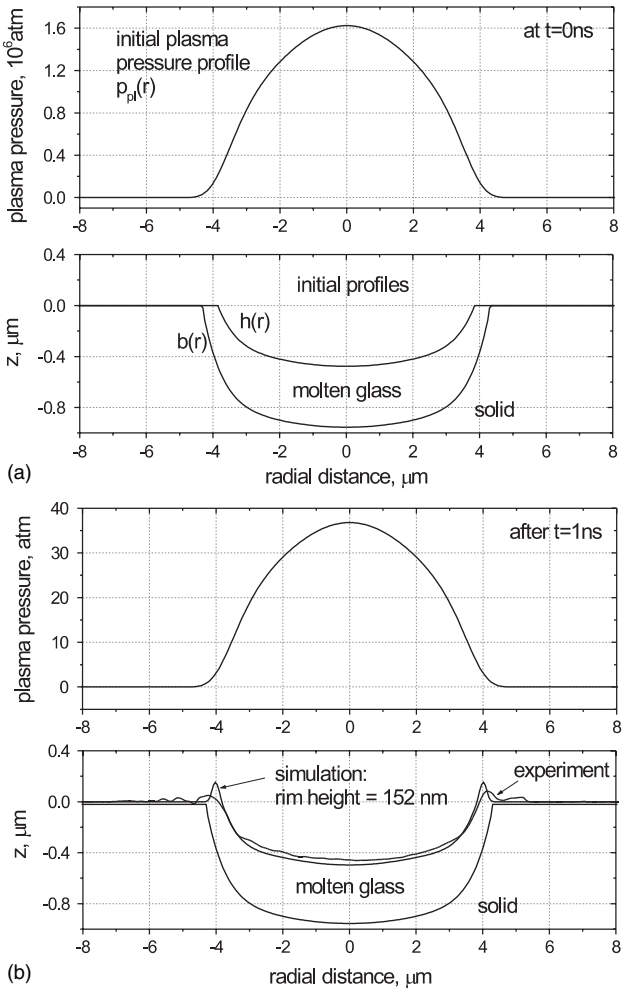

Figure 10. Numerical solutions of pressure-driven melt flow for $\mu = 2$ Pa s and $w_0 = 5.9\,\mu$m. The top plot shows the plasma pressure and the bottom plot shows the evolution of the free surface after $t = 1$ ns. The measured profile of the ablation crater is added for comparison of the rim height.

For comparison, we have also plotted the measured ablation crater profile. After 1 ns the rim height reaches a plateau and does not increase anymore as the plasma pressure decreases below tens of atmospheres.

The numerical results shown in figure 10 indicate that a tall rim (≈150 nm) can be formed within the first nanoseconds of the ablation process. Femtosecond laser generated plasmas exhibit very high pressures (millions of atm) in the first tens of picosecond. As the plasma expands mainly in 1D, the pressure drops quickly to a several tens of atm within a few tens of nanoseconds [19]. During this time, the plasma pressure gradient is especially high at the periphery pushing the molten layer underneath the plasma and forming an elevated rim surrounding the ablation crater. This high aspect ratio rim will eventually tilt outwards because of the pressure difference between the high pressure plasma inside and the atmospheric air pressure outside. This hypothesis can further be supported with a high resolution SEM image of a rim shown in figure 11. This image clearly suggests that the rim is a resolidified splash of a very tall rim surrounding the ablation crater.

Since there is a lack of experimental data available for the viscosity of molten glass in the high-temperature regime, we

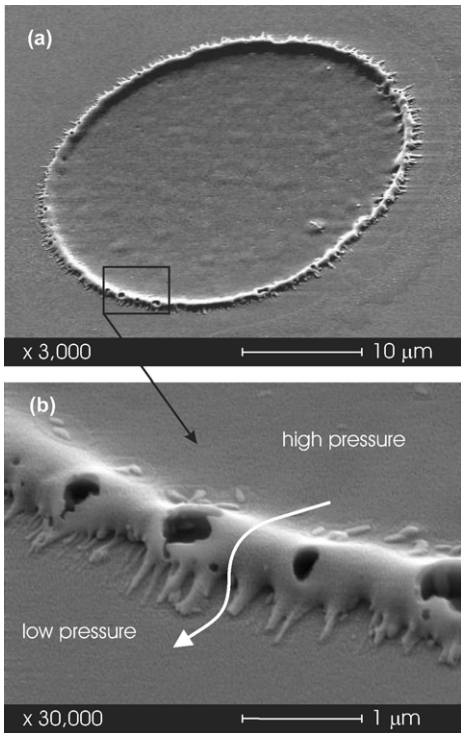

Figure 11. SEM images of a crater generated with a single 800 nm and 100 fs laser pulse. (*a*) The whole crater at 3000× magnification and (*b*) a higher resolution SEM image (30 000× magnification) focused on the rim formed around the crater. The laser fluence was $F_0^{\rm avg} = 34\,{\rm J\,cm^{-2}}$.

estimate the glass viscosity by extrapolating the available data at lower temperatures. The estimates indicate that for temperatures above 2500 K, the glass viscosity would be between 1 and 10 Pa s or even less. The simulations results for $\mu = 10$ Pa s shows that a rim of 30 nm height gets accumulated around the ablation crater within 1 ns after the plasma is formed. The rim becomes very tall for a lower value of viscosities, reaching up to 500 nm for $\mu = 0.5$ Pa s.

4.3.4. Time scales of various processes after rim formation. Once a rim (bump) is formed around the crater, it may relax down in the absence of the pressure-induced driving forces. We will next examine the bump relaxation time scale with comparison to its solidification time scales.

- The time scale to relax a bump of a height $\ell = 150$ nm is $\ell\mu/\gamma \approx 1\,\mu$s.
- The time scale to solidify a bump depends on the thermal conductivity and radiative cooling. The time scale associated with radiative cooling is proportional to σT^4 where σ is the Stefan–Boltzmann constant. Hence, the time scale for the radiative cooling of a bump with a horizontal length scale of $\ell_{\rm w} = 400$ nm is $\ell_{\rm w}\rho C_p \Delta T/\sigma T^4 \approx 20\,\mu$s. On the other hand, the time scale associated with conductivity is proportional to $(\ell_{\rm w})^2\rho C_{\rm p}/k \approx 100$ ns. Thus, the bump will resolidify through heat conduction before it will relax down. Furthermore, the melt will cool even more rapidly near the edges since the heat flow is higher near regions of rapid variations (the edges).

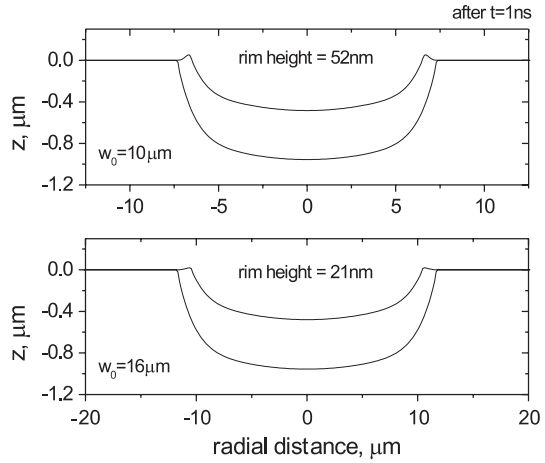

Figure 12. The free surface evolution after $t = 1$ ns for two different beam diameters; $w_0 = 10\,\mu$m (the top plot) and $w_0 = 20\,\mu$m (the bottom plot). In these calculations $\mu = 2$ Pa s. The rim height decreases as the diameter of the crater becomes larger.

In conclusion, our simulations are suggestive that we are capturing, overall, the right physical processes. There are missing details, due to the complication of the physics and geometry, that would need to be known much more accurately to get the simulation closer to measurements. These semi-quantitative calculations thus do not present an exact solution for the problem but a qualitative description of how the plasma pressure affects the crater and rim formation and estimates for the time scales that are important.

4.4. How to suppress the rim formation?

We can now answer the question of 'how to suppress the rim formation for clean laser processing' or in other words seek 'how to achieve clean borders of the irradiated spot'.

If the pressure-driven flow time, τ_p, is long enough, the pressure-induced forces acting on the fluid will not be able to drive the molten material from the centre to the edges of the crater during the short lifetime of the high pressure plasma. From the parametric dependence of τ_p shown in equation (19), the rim height depends on

$$\text{rim height} \;\propto\; \frac{\langle p_{pl}\rangle \langle h_m\rangle^2}{\mu L^2}. \tag{31}$$

During experiments, we can control two of these parameters; the melt thickness, $\langle h_m\rangle$, and the characteristic length scale, L, by varying the laser beam radius w_0. Smaller melt thickness or larger beam radius (wider ablation crater) will both lead to smaller rim heights. The initial melt thickness is proportional to $h_{m,0} \propto \alpha_{eff}^{-1} \ln(AF_{th}/\rho C p \alpha_{eff}^{-1}(T_m - T_0))$. Therefore a thinner melt thickness can be achieved by reducing the optical penetration depth by using shorter laser wavelengths or/and shorter pulse durations. Both the melt thickness and lifetime will be further reduced by the decreased amount of the absorbed thermal energy ($F_{heat} \propto F_{th}$) because the threshold fluence decreases with both laser wavelength and pulse duration [11, 25].

Figure 12 illustrates the effect of the crater dimensions. Here, we plot the evolution of the free surface after $t = 1$ ns for two different laser beam spot sizes. As the ablation crater gets larger it takes longer to drive the fluid from the crater centre to the edges. It may be even possible to achieve a negligible rim height by increasing the width of the ablation crater.

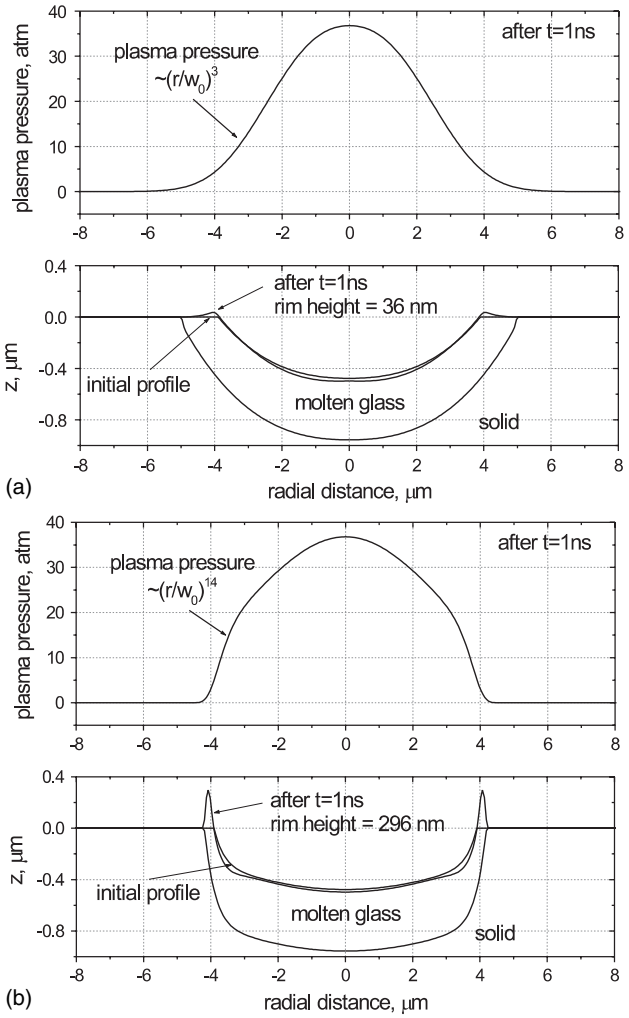

Figure 13. The free surface evolution after $t = 1$ ns for two different effective beam profiles.
(*a*) $F_{eff}(r) \propto \exp\{-2[(r/w_0)^2 + (r/0.8w_0)^3]\}$ and
(*b*) $F_{eff}(r) \propto \exp\{-2[(r/w_0)^2 + (r/0.68w_0)^{14}]\}$. In these calculations $w_0 = 5.9\,\mu$m and $\mu = 2$ Pa s. The rim height decreases as the steepness of the effective beam profile decreases.

Another way of suppressing the rim formation may be by modifying the effective laser beam profile. As shown in figure 13(*a*), with a less steep effective laser profile the formation of a rim takes longer time. On the other hand, for a steeper effective beam profile, the elevated rim becomes taller (see figure 13(*b*)). Therefore, if one can modify the laser spatial beam profile, it may be possible to achieve a cleaner border of the irradiated spot. Although it is easy to control the intensity distribution of the laser beam profile, it is not clear, however, how this may impact the pressure distribution in the plasma. This remains a subject for further investigation.

5. Conclusions

The morphology of the single-shot ablated areas revealed a smooth and shallow crater surrounded by an elevated

rim. From these experimental observations, conclusions could be drawn about the ablation mechanism of borosilicate glass. We argued that a very thin melt zone existed during the ablation process and calculated the thermal and flow properties of this thin melt zone. In these calculations, several characteristic time constants associated with ablation, melting and flow processes were determined. The comparative values revealed that a flow of fluid driven by a plasma-induced pressure gradient localized near the radius of the laser pulse, with reasonable values of the plasma pressure, would have enough time to move melted material towards the edge and so deposit a thin rim around the ablated area. Physically based estimates of the melt thickness and the pressure-driven flow process then suggest ways to suppress this rim formation.

Acknowledgments

The authors gratefully acknowledge the contributions of Professor Eric Mazur and Dr Mengyan Shen to this investigation.

Appendix A. Derivation of the equation of motion for the thin-film model

In this appendix we present a short derivation of the partial differential equation describing viscous fluid flow in a thin film [17, 18, 24]. Suppose that the position of the free surface of the fluid is denoted as $z = h(x, y, t)$, and the shape of the time-independent bottom substrate is denoted as $z = b(x, y, t)$. We assume that the flow is incompressible and described by the Navier–Stokes equations. Then, the fluid velocity $\boldsymbol{u}$ and pressure p satisfy

$$\frac{\partial \boldsymbol{u}}{\partial t} + \boldsymbol{u}\cdot\nabla\boldsymbol{u} = -\frac{1}{\rho}\nabla p + \frac{\mu}{\rho}\nabla^2\boldsymbol{u}, \tag{A1}$$

$$\nabla\cdot\boldsymbol{u} = 0. \tag{A2}$$

For some of the estimates below, it is convenient to denote the mean film thickness $h_{\mathrm{m}} = O(h-b)$ and the average, or typical, fluid pressure by $\langle p\rangle$. Note that in (A1) we are neglecting the gravitational body force since for the small length scales characteristic of the rims in the experiments, $\rho g h_{\mathrm{m}}/\langle p\rangle \ll 1$. The boundary conditions to be satisfied are no slip on the solid substrate, the normal and tangential stress balances across the free surface and the kinematic boundary condition on the free surface.

For pressure-driven flows on the scale L typical of the flow direction, we expect a typical velocity along the film to have magnitude $u = O(h_{\mathrm{m}}^2\langle p\rangle/(\mu L))$, in which case we define the Reynolds number for the thin-film flow as $\mathcal{R}_e = \rho h_{\mathrm{m}}^3\langle p\rangle/(\mu^2 L)$. Let us suppose first that the velocity field is $\boldsymbol{u}(x, y, z, t) = (u, v, w)$. Then, under the thin-film (lubrication) approximation we assume $h_{\mathrm{m}}/L \ll 1$ and inertial effects are negligible, which is equivalent to the requirement that the Reynolds number is small, $\mathcal{R}_e \ll 1$, so that the Navier–Stokes and continuity equations reduce to

$$\nabla_2 p = \mu\frac{\partial^2\boldsymbol{u}_2}{\partial z^2}, \tag{A3}$$

$$\frac{\partial p}{\partial z} = 0, \tag{A4}$$

$$\nabla_2\cdot\boldsymbol{u}_2 + \frac{\partial w}{\partial z} = 0, \tag{A5}$$

where $\nabla_2 = (\partial_x, \partial_y)$ and $\boldsymbol{u}_2 = (u, v)$. Within the lubrication approximation, the boundary conditions are

$$p = p_{pl} - \gamma\kappa \qquad \text{on } z = h \text{ (normal stress)}, \tag{A6}$$

$$\mu\frac{\partial u}{\partial z} = \nabla_2\gamma \qquad \text{on } z = h \text{ (tangential stress)}, \tag{A7}$$

$$u = v = w = 0 \qquad \text{on } z = b \text{ (no slip)}, \tag{A8}$$

$$\frac{\partial h}{\partial t} + \boldsymbol{u}_2\cdot\nabla_2 h - w = 0 \qquad \text{on } z = h \text{ (kinematic condition)}, \tag{A9}$$

where p_{pl} is the plasma pressure above the free surface, γ is the surface tension of the interface and κ is twice the mean curvature of the interface.

Equation (A4) and the normal stress balance give the local pressure in the liquid to be

$$p = p_{\mathrm{pl}} - \gamma\kappa, \qquad b(x, y) \leqslant z \leqslant h(x, y, t) \tag{A10}$$

and we will use a linearized expression for the mean curvature term, $\kappa = \nabla_2^2 h$, where ∇_2 is the two-dimensional gradient operator. Substituting the pressure in equation (A3), integrating the result twice with respect to z and using the no slip and tangential stress boundary conditions yields

$$\boldsymbol{u}_2 = \frac{1}{\mu}\left(\frac{z^2}{2} - \frac{b^2}{2} + bh - zh\right)\left(\nabla_2 p_{\mathrm{pl}} - \nabla_2(\gamma\nabla_2^2 h)\right) + \frac{1}{\mu}(z-b)\nabla_2\gamma, \tag{A11}$$

where $\boldsymbol{u}_2$ in the equation (A11) is the velocity distribution in the plane of the glass.

Integrating the continuity equation shows that

$$\frac{\partial h}{\partial t} + \nabla_2\cdot\boldsymbol{q} = 0 \qquad \text{with} \quad \boldsymbol{q} = \int_{z=b}^{z=h}\boldsymbol{u}_2\,\mathrm{d}z, \tag{A12}$$

where $\boldsymbol{q}$ is the flux vector. Substituting (A11) for $\boldsymbol{u}_2$ to calculate the depth-averaged flux, $\boldsymbol{q}$, we then obtain the evolution equation for the height, h, of the thin film:

$$\frac{\partial h}{\partial t} + \nabla_2\cdot\left[\frac{(h-b)^2}{2\mu}\nabla_2\gamma - \frac{(h-b)^3}{3\mu}\left(\nabla_2 p_{\mathrm{pl}} - \nabla_2(\gamma\nabla_2^2 h)\right)\right] = 0. \tag{A13}$$

In cylindrical coordinates and assuming an axisymmetric shape, $h(r, t)$, equation (A13) becomes

$$\frac{\partial h}{\partial t} + \frac{1}{r}\frac{\partial}{\partial r}r\left[\frac{(h-b)^2}{2\mu}\frac{d\gamma}{dr} - \frac{(h-b)^3}{3\mu}\frac{dp_{\mathrm{pl}}}{dr} + \frac{(h-b)^3}{3\mu}\frac{\partial}{\partial r}\left(\frac{\gamma}{r}\frac{\partial}{\partial r}\left(r\frac{\partial h}{\partial r}\right)\right)\right] = 0. \tag{A14}$$

References

[1] Ameer-Beg S, Perrie W, Rathbone S, Wright J, Weaver W and Champoux H 1998 Femtosecond laser microstructuring of materials *Appl. Surface Phys.* **127–129** 875–80

[2] Ben-Yakar A and Byer R L 2004 Femtosecond laser ablation properties of borosilicate glass *J. Appl. Phys.* **96** 5316

[3] Ben-Yakar A, Byer R L, Harkin A, Ashmore J, Stone H A, Shen M and Mazur E 2003 Morphology of femtoseocnd laser ablated borosilicate glass surfaces *Appl. Phys. Lett.* **83** 3030–2

[4] Born M and Wolf E 1999 *Principles of Optics* 7th edn (Cambridge: Cambridge University Press)

[5] Cahn R W, Haasen P and Kramer E J 1998 *Materials Science and Technology: A Comprehensive Treatment* (New York: Wiley)

[6] Choi T Y and Grigoropoulos C P 2002 Plasma and ablation dynamics in ultrafast laser processing of crystalline silicon *J. Appl. Phys.* **92** 4918–25

[7] Chowdhury I H, Wu A Q, Xu X and Weiner A M 2005 Ultra-fast laser absoprtion and ablation dynamics in wide-band-gap dielectrics *Appl. Phys.* A **81** 1627–32

[8] Lide D R (ed) 1999–2000, *CRC Handbook of Chemistry and Physics* 80th edn (Boca Raton, FL: CRC Press)

[9] Doremus R H 1994 *Glass Science* 2nd edn (New York: Wiley)

[10] Itina T E, Vidal F, Delaporte P and Sentis M 2004 Numerical study of ultra-short laser ablation of metals and of laser plume dynamics *Appl. Phys.* A **79** 1089–92

[11] Jia T Q, Xu Z Z, Li R X, Shai B and Zhao F L 2003 Microscopic mechanisms of ablation and micromachining of dielectrics by using femtosecond lasers *Appl. Phys. Lett.* **82** 4382–4

[12] Kingery W D 1959 Surface tension of some liquid oxides and their temperature coefficients *J. Am. Ceram. Soc.* **42** 6–10

[13] Ladieu F, Martin P and Guizard S 2002 Measuring thermal effects in femtosecond laser-induced breakdown of dielectrics *Appl. Phys. Lett.* **81** 957–9

[14] Laville S, Vidal F, Johnston T W, Chaker M, Le Drogoff B, Berthélemy O, Margot J and Sabsabi M 2004 Modeling the time evolution of laser-induced plasmas for various pulse durations and fluences *J. Plasmas* **11** 2182–90

[15] Mao S S, Quéré F, Guizard S, Mao X, Russo R E, Petite G and Martin P 2004 *Appl. Phys.* A **79** 1695

[16] Meijer J, Du K, Gillner A, Hoffmann D, Kovalenko V S, Masuzawa T and Ostendorf A 2002 Laser machining by short and ultrashort pulses, state of the art *Ann. CIRP* **51/2/2002** 1–20

[17] Myers T G 1998 *SIAM Rev.* **40** 441

[18] Oron A, Davis S H and Bankoff S G 1997 *Rev. Mod. Phys.* **69** 931

[19] Perry M D, Stuart B C, Banks P S, Feit M D, Yanovsky V and Rubenchik A M 1999 Ultrashort-pulse laser machining of dielectric materials *J. Appl. Phys.* **85** 6803–10

[20] Schaffer C B, Brodeur A and Mazur E 2001 Laser-induced breakdown and damage in bulk transparent materials induced by tightly focused femtosecond laser pulses *Meas. Sci. Technol.* **12** 1784–94

[21] Schwarz-Selinger T, Cahill D G, Chen S C, Moon S J and Grigoropoulos C P 1999 Micron-scale modifications of si surface morphology by pulsed-laser texturing *Phys. Rev.* B **64** 155323

[22] Sen S and Dickinson J E 2003 Ab initio molecular dynamics simulation of femtosecond laser-induced structural modification in vitreous silica *Phys. Rev.* B **68** 214204

[23] Sokolowski-Tinten K, Bialkowski J, Cavalleri A, von der Linde D, Oparin A, ter Vehn J M and Anisimov S I 1998 Transient states of matter during short pulse laser ablation *Phys. Rev. Lett.* **81** 224–7

[24] Stone H A 2002 Partial differential equations in thin film flows in fluid dynamics: spreading droplets and rivulets *Nonlinear PDE's in Condensed Matter and Reactive Flows* ed H Berestycki and Y Pomeou p 297

[25] Stuart B C, Feit M D, Herman S, Rubenchik A M, Shore B W and Perry M D 1996 Ultrashort-pulse laser machining of dielectric materials *Phys. Rev.* B **53** 1749–61

[26] Tokarev V N and Kaplan A F H 1999 Suppression of melt flows in laser ablation: application to clean laser processing *J. Phys. D: Appl. Phys.* **32** 1526–38

[27] Vázquez de Aldana J R, Méndez C, Roso L and Moreno P 2005 Propagation of ablation channels with multiple femtosecond laser pulses in dielectrics: numerical simulations and experiments *J. Phys. D: Appl. Phys.* **38** 2764–7

[28] Vidal F, Laville S, Johnston T W, Barthelemy O, Chaker M, Le Drogoff B, Margot J and Sabsabi M 2001 Numerical simulations of ultrashort laser pulse ablation and plasma expansion in an ambient air *Spectrochim. Acta* B **56** 973–86

[29] Laville S, Vidal F, Johnston T W, Chaker M, Le Drogoff B, Barthélemy O, Margot J and Sabsabi M 2001 Modeling the time evolution of laser-induced plasmas for various pulse durations and fluences *Phys. Plasmas* **11** 2182–90

[30] Willis D A and Xu X 2000 Transport phenomena and droplet formation during pulsed laser interaction with thin films *J. Heat Transfer* **122** 763–70

[31] Zeng X, Mao X L, Greif R and Russo R E 2005 Experimental investigation of ablation efficiency and plasma expansion during femtosecond and nanosecond laser ablation of silicon *Appl. Phys.* A **80** 237–41

[32] Zhidkov A G, Zhigilei L V, Sasaki A and Tajima T 2001 Short-laser-pulse-driven emission of energetic ions into a solid target from a surface layer spalled by a laser prepulse *Appl. Phys.* A **73** 741–7

[33] Zhigilei L V and Garrison B J 2000 Microscopic mechanisms of laser ablation of organic solids in the thermal and stress confinement irradiation regimes *J. Appl. Phys.* **88** 1281–98